Journal of Cleaner Production 428 (2023) 139434

Contents lists available at ScienceDirect

Journal of Cleaner Production

journal homepage: www.elsevier.com/locate/jclepro

Capture of NH_3 using air plasmas to form NH_4NO_3 for N recycling: Impact factors and mechanisms

Mengqi Li, Zhenguo Hou, Yi Dai, Zhuocheng Song, Zilan Xiong *

State Key Laboratory of Advanced Electromagnetic Technology, Huazhong University of Science and Technology, Wuhan, Hubei, 430074, People's Republic of China

ARTICLE INFO

Handling Editor: Jin-Kuk Kim

Keywords:
Air plasma
Ammonia capture
Nitrogen fixation
NH_4NO_3

ABSTRACT

Ammonia loss results in significant resource waste and environmental pollution. In this study, we proposed and explored the way of using air plasmas to capture NH_3 to form NH_4NO_3 for N recycling under different reaction modes, discharge powers, and gas flow rates. The reaction mechanisms under different modes were also revealed. A needle-needle discharge driven by AC power was used and ammonia gas was utilized to simulate the volatilized ammonia. Notably, white particles were observed during Mode 1 and Mode 2 (these particles gradually disappeared over time in Mode 2), while no particles or significant NO_x were detected in Mode 3 throughout the process. The quantitative NH_4NO_3 yield was significantly influenced by discharge power and NH_3 flow rate, reaching its highest value in Mode 1 at 24 W and 20 sccm in this investigation. Directly mixing the air discharge products with NH_3 in Mode 1 under the threshold decomposition temperature of NH_4NO_3 leads to the stable formation of NH_4NO_3. Discharging in the NH_3/air mixture will inhibit the generation of NO_x and further restrain the NH_4NO_3 formation in Mode 2 and 3. Additionally, the temperature rises during discharge and also decomposes NH_4NO_3, resulting in unstable NH_4NO_3 formation in Mode 2.

1. Introduction

Nitrogen is an essential element for all living organisms (Fowler et al., 2015; Galloway et al., 2004), however, low nitrogen utilization efficiency (NUE) and high loss rates bring challenges in terms of energy conservation and environmental protection (Congreves et al., 2021). In agriculture and livestock, nitrogen loss primarily occurs in the form of N_2O and NH_3, which dominants among the various ways of N loss (Bouwman et al., 2013; Fowler et al., 2013). Among these, the NH_3 emission from livestock (animal house and manure storage area) contributes to over 80% of NH_3 emissions from agricultural and pastoral systems (Anderson et al., 2003; Fowler et al., 2013, 2015). The excessive release of NH_3, a toxic and irritating gas, not only leads to air pollution but also poses a threat to human health (Park et al., 2021). Therefore, improving NUE and reducing NH_3 emissions have become focal points in addressing this issue (Chojnacka et al., 2021; Panetta et al., 2005).

Plasma technology, known for its low pollution, high energy utilization efficiency, and flexibility (Chen et al., 2021; Patil et al., 2015), has emerged as a promising alternative to the traditional energy-intensive and polluting Haber-Bosch (H–B) method of nitrogen fixation (Humphreys et al., 2021). Current plasma nitrogen fixation methods focus on reducing energy costs and producing nitrogen oxides or ammonia from the air or other gas mixtures such as N_2/O_2 or N_2/H_2 (Pei et al., 2019; Peng et al., 2018; Zhou et al., 2021). Different catalysts have also been introduced in these processes to improve synthesis efficiency (Akay, 2017; Hong et al., 2018). Although the theoretical energy consumption of plasma nitrogen fixation is lower than that of the H–B method, there remains a significant gap between the laboratory results and the theoretical value (Chen et al., 2021; Patil et al., 2015).

Furthermore, the discharge plasma has also been used to reduce the ammonia emissions from industrial wasted gas/water (Wang et al., 2015). In earlier researches, the removal of NH_3 was typically achieved through direct discharge in NH_3 or ammonia-containing waste gases (Tanthapanichakoon et al., 2004; Xia et al., 2008). Gas-phase and liquid-phase plasmas have been subsequently developed for the removal of ammonia nitrogen in wastewater (Back et al., 2023; Fan et al., 2021; Wu et al., 2021). Additionally, catalysts have been widely introduced into reaction systems. Researchers have further dedicated their efforts to improving the efficiency of ammonia removal and exploring methods for its conversion into valuable and reusable products, such as hydrogen (Chung et al., 2022; Wang et al., 2015; Zhang and Wang, 2016).

Both plasmas for nitrogen fixation and ammonia removal contribute

---

* Corresponding author.
E-mail address: zilanxiong@hust.edu.cn (Z. Xiong).

https://doi.org/10.1016/j.jclepro.2023.139434
Received 27 July 2023; Received in revised form 6 October 2023; Accepted 19 October 2023

to the nitrogen cycle. Given that the main NH_3 emission into the air comes from agriculture and livestock, direct decomposing of NH_3 would result in significant energy loss. If the wasted NH_3 could be captured during the air plasma nitrogen fixation process in the form of NH_4NO_3 (a high-nitrogen fertilizer with an N content of 34%), it would substantially reduce the energy cost of plasma nitrogen fixation and also offer benefits for environmental protection. However, it was found in some literature that during the utilization of plasma for ammonia removal, white powder byproduct was also found on the inner wall of the reactor chamber during the direct reaction mode between plasma and NH_3 (Tanthapanichakoon et al., 2004; Vervloessem et al., 2023; Xia et al., 2008). This byproduct is speculated to be NH_4NO_3. Therefore, how to effectively capture NH_3 for stable NH_4NO_3 formation using air plasma (direct reaction or indirect reaction with plasma) becomes a key issue. Furthermore, the discharge power will strongly influence the reactions and determine the products in plasma (Mei and Tu, 2017; Xie et al., 2020). The gas flow rate (or gas concentration) also plays a crucial role and is an important factor that affects the reaction rate and residence time in the reaction zone as well as the sufficiency of the reaction (Chang et al., 2021; Zhu et al., 2016).

Based on the idea and discussion above, we proposed and explored the way of using air plasmas to capture NH_3 to form NH_4NO_3 for N recycling. Especially, the influence of the reaction modes, plasma discharge power (NO_x concentration), and NH_3 flow rate (NH_3 concentration) on the capture efficiency were studied. A needle-needle discharge device driven by AC sources was used to generate the plasma under different discharge powers. Three reaction modes were introduced: the indirect reaction mode (Mode 1), the mixed reaction mode (Mode 2), and the direct reaction mode (Mode 3) to explore the appropriate way for the plasma to capture NH_3. The images of the phenomenon within the reaction chamber, the optical emission spectroscopy (OES) of the discharge, and the gas phase Fourier-transform infrared (FTIR) of the products were recorded, measured, and quantitatively analyzed. Solid NH_4NO_3 particles were collected at different reaction times using a filter membrane and weighed for comparison under different reaction modes, discharge power, and NH_3 flow rates. Based on the experimental results, the underlying reaction mechanisms for each mode were also discussed and summarized.

2. Experimental setup and measurements

2.1. Experimental setup

The sketch of the experimental setup is shown in Fig. 1. Inside an acrylic chamber with inner dimensions of 10 cm × 10 cm × 10 cm, a pair of stainless-steel needle electrodes are fixed 2 cm above the bottom to generate plasma. The distance between the needle tips is fixed at 5 mm. A quartz window (30 mm × 30 mm × 2 mm) is installed on one side wall for OES detection, while a pair of parallel ZnSe windows (⌀15 × 2 mm) is mounted on the other two opposite side walls for FTIR detection. A high voltage AC power supply (CTP-2000K, Corona Lab, China) drives the discharge device, with the discharge power set at 8, 16, and 24 W respectively. The gas inlet of the chamber is connected to a mass flow controller (MKS 1479A, USA) for flow rate regulation, and the gas outlet is connected to a gas filter equipped with a PTFE filter membrane of 0.1 μm. This filter is connected to an air pump to collect the particulate matter. The white particles on the chamber walls are collected by scraping. All the collected particles are weighed after vacuum drying in an oven.

The schematic diagram of the three reaction modes employed in this experiment is shown in Fig. 2. In Mode 1, an indirect reaction mode, the discharges are operated in the air for 5 min. After that, the plasma is turned off, and NH_3 is injected into the chamber at a rate of 80 mL/min for an additional 5 min to react with the air plasma products. In Mode 2, the initial 5 min is identical to Mode 1, followed by injecting NH_3 at a rate of 80 mL/min into the chamber for 5 min while the discharge is on. In Mode 1 and Mode 2, air is not introduced into the chamber, and the air inside the chamber is used. In Mode 3, the discharge keeps on throughout the entire process in the mixture of air at a rate of 500 mL/min and NH_3 at a rate of 80 mL/min.

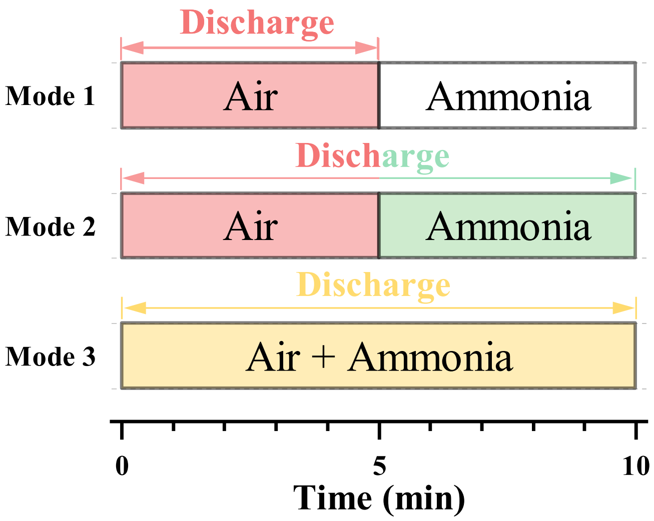

Fig. 2. Schematic diagram of the three reaction modes employed in the experiment.

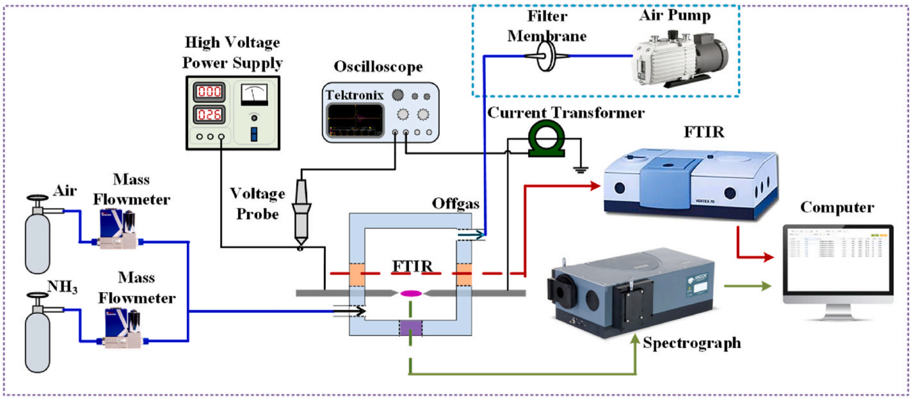

Fig. 1. Sketch of the experiment setup.

2.2. Electrical and optical diagnosis

For the measurement and recording of discharge voltage and current, an oscilloscope DPO3034 (Tektronix, USA) equipped with a voltage probe P6015A (Tektronix, USA) and current transformer P6585 (Pearson, USA) was utilized. The discharge power was obtained by calculating the periodic average of the integration of discharge voltage and current.

The OES analysis was conducted using a spectrometer SR-500I-A (Andor, UK) coupled with a photomultiplier tube PMTH-S1 (Zolix, China). Throughout the experiment, a fiber optic adapter was equipped in the spectrometer, and a 1200-I/mm grating was selected to capture the spectrum within the wavelength range of 200–800 nm. Specifically, the spectrum of the N_2 second positive system ($C_3\Pi_u$ - $B_3\Pi_g$) in the range of 368–382 nm was utilized to fit the rotational temperature (T_r) and vibrational temperature (T_v), which was measured with a 2400-I/mm grating to achieve higher accuracy. At atmospheric pressure, T_r is generally considered to be approximately equal to the gas temperature upon discharging (Engeln et al., 2020).

2.3. Products detection

Gas-phase products in the chamber were identified using an FTIR spectrometer Vertex 70 (Bruker, Switzerland). The gas concentration was quantitatively determined by fitting the obtained spectra with an FTIR database established by the laboratory, following the principles of the Lambert-Beer law (Mayerhöfer et al., 2020).

Particulate matter was generated under specific experimental conditions in the chamber. To quantitatively measure the particulate matter, samples were collected at 6 min, 8 min, and 10 min in all three modes. The sampling duration for particulate matter is 1 min, and after each sampling, a new experiment was conducted to collect the next data point. The collected particles were weighed using an analytical balance (AB135-S, METTLER TOLEDO, Switzerland) with a precision of 0.01 mg. Each time point was tested separately and repeated at least three times to ensure accuracy and reproducibility.

The particulate matter was further characterized using scanning electron microscopy (SEM), energy dispersive spectroscopy (EDS), and attenuated total reflection Fourier-transform infrared spectroscopy (ATR-FTIR) techniques. The microstructure and elemental composition were analyzed using a field emission scanning electron microscope (FE-SEM) GeminiSEM300 (Carl Zeiss, Germany) equipped with a high-sensitivity secondary electron detector and an EDS AZtec X-Max 50 (Oxford, UK). Additionally, an ATR apparatus was equipped with the FTIR spectrometer to identify the components within the wavenumber range of 4000–500 cm^{-1}.

3. Experimental results

3.1. Electrical and optical parameters

Fig. 3 shows the discharge images of all modes and the typical voltage and current waveforms under different discharge power levels. The discharge images clearly illustrate that as the discharge power increases, the discharge becomes more intense, resulting in a stronger emission of light. Notably, due to variations in the gas environment during the discharge process, the color of the emitted light exhibits a gradual transition from pale purple to intense orange as the discharge power increases, observed during the 0–5 min period in Modes 1 and 2, as well as throughout the discharge in Mode 3. Additionally, during the 5–10 min in Mode 2, the emitted light undergoes a color transition from golden yellow to pale purple as the discharge power increases. These distinctive discharge images effectively capture the discrepancies in discharge states across the different modes.

Fig. 4 illustrates the OES obtained during discharging with a power of 8 W in all three modes. N_2(C–B) in the range of 295–450 nm (Cicala et al., 2009; Es-Sebbar et al., 2009; Suraj et al., 2007), N_2(B-A) in the range of 493–800 nm (Es-Sebbar et al., 2009; Lofthus and Krupenie, 1977; Suraj et al., 2007), N_2^+(B-X) around 391.4, 427.8, 470.9 nm (Chen and Li, 2017; Suraj et al., 2007), N_2^+(A-X) around 782 nm (Suraj et al., 2007), and H_α around 656.3 nm (Suraj et al., 2007) are all presented. Comparing the intensity of these peaks across different modes, it is observed that Mode 2 (5–10 min) and Mode 3 exhibited relatively lower intensities compared to air discharge (Modes 1 and 2, 0–5 min). In Mode 2 (5–10 min), the emergence of distinctive NH(A-X) emission lines (at around 336.1 nm) (Chen and Li, 2017; Suraj et al., 2007; Yi et al., 2017) and N (around 672 nm) (Clay et al., 1996) are observed. However, no significant OH(A-X) and O emissions are presented in Mode 2 (5–10 min) (Bruggeman et al., 2012; Machala et al., 2007). These changes can be attributed to a significant transfer of discharge energy towards the excitation of NH_3 molecules, resulting in a decreased intensity of N_2, O_2, and H_2O-related emissions.

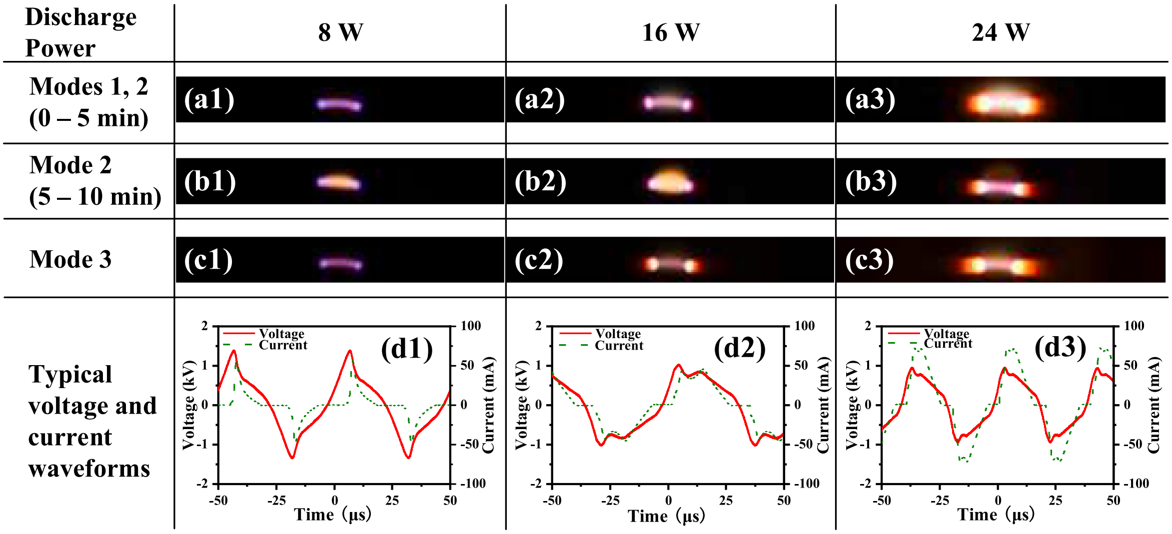

Fig. 3. Discharge images of (a) Mode 1 and 2 (0–5 min), with the discharge power of (a1) 8 W, (a2) 16 W, and (a3) 24 W; (b) Mode 2 (5–10 min), with the discharge power of (b1) 8 W, (b2) 16 W, and (b3) 24 W; (c) Mode 3 (0–10 min), with the discharge power of (c1) 8 W, (c2) 16 W, and (c3) 24 W. (d) Typical voltage and current waveforms of Mode 1 (0 – 5min), (d1) 8 W, (d2) 16 W, (d3) 24 W.

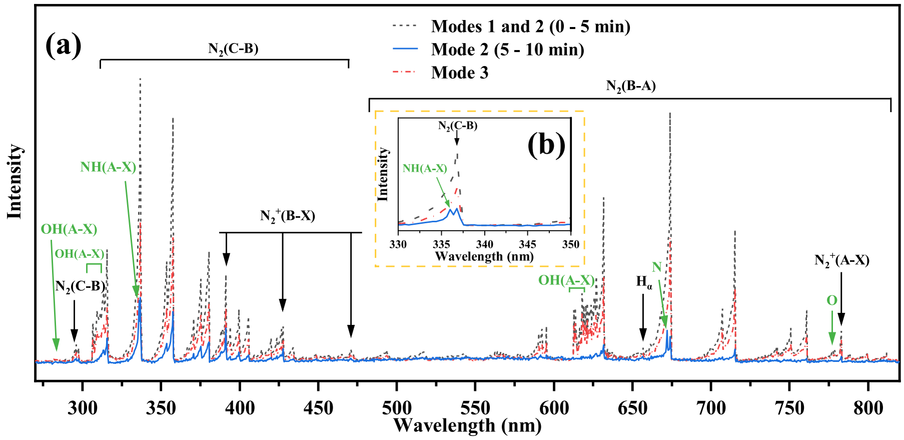

Fig. 4. OES with the discharge power of 8 W in the range of (a) 270–820 nm, and (b) 330–350 nm to show the spectral lines of NH (A–X).

At higher discharge powers, no new species is detected, but the intensity increases with the power. It is important to note that as the discharge gradually transitioned to an arc discharge, the OES analysis of the plasma region was affected by a background spectrum caused by blackbody radiation emitted from the electrodes at high temperatures (Nishio et al., 2004). Therefore, the OES results presented in Fig. 4 for the power of 8 W serve as an illustrative example for further analysis.

3.2. *Temperature change and attendant phenomena inside the chamber*

The vibrational temperature T_v of plasma affects the vibrational excitation states of gas molecules and is crucial for the original reaction processes and products in the plasma region. The rotational temperature T_r of plasma can be approximately equivalent to the gas temperature in the discharge area, and subsequently determines the temperature distribution in the reaction chamber. Both the T_v and T_r will significantly affect the reactions and product formation inside the reaction chamber. Fig. 5 (a) illustrates the spectrum fitting results for T_v and T_r for air discharge under 24 W. In Modes 1 and 2 (0–5 min), the gas temperature, represented by T_r, remains around 2300 K. Similarly, under other discharge conditions, the gas temperature also remains within the range of 2300 (±200) K, as listed in Appendix A. With decreasing power, the gas temperature slightly decreases, while the injection of NH_3 during discharge leads to a slight increase in gas temperature. Fig. 5 (b) shows the temperature changes over time at different positions away from the discharge region under various modes at 24 W. During the initial 0–5 min, the temperature changes in Modes 1 and 2 are identical. At a distance of 2 cm from the discharge region, the temperature remains around 420 (±10) K, which is approximately 65 K higher than the temperature around 355 (±5) K at a distance of 5 cm. However, after 5 min, the temperature in Mode 1 sharply drops to 306 (±5) K at different distances, while in Mode 2, the temperature significantly increases, reaching 502 (±51) K at a distance of 2 cm and 362 (±5) K at a distance of 5 cm. For Mode 3, the temperature at different positions remains relatively constant, with a temperature of 495 (±50) K at a distance of 2 cm and 368 (±20) K at a distance of 5 cm from the discharge region.

The phenomena occurring within the chamber under 24 W are presented in Fig. 6. From Fig. 6 (a) and (b), it can be observed that within 0–5 min, the reddish-brown gas gradually increases inside the chamber as time progresses. After 5 min of reaction in Mode 1, when NH_3 was injected and the discharge was turned off, there was clear evidence of “white smoke” inside the chamber. At 6 min (as shown in Fig. 6 (a4)), it can still be seen that the “white smoke” mixes with the reddish-brown gas. After 8 min, the reddish-brown gas is no longer visible, and the

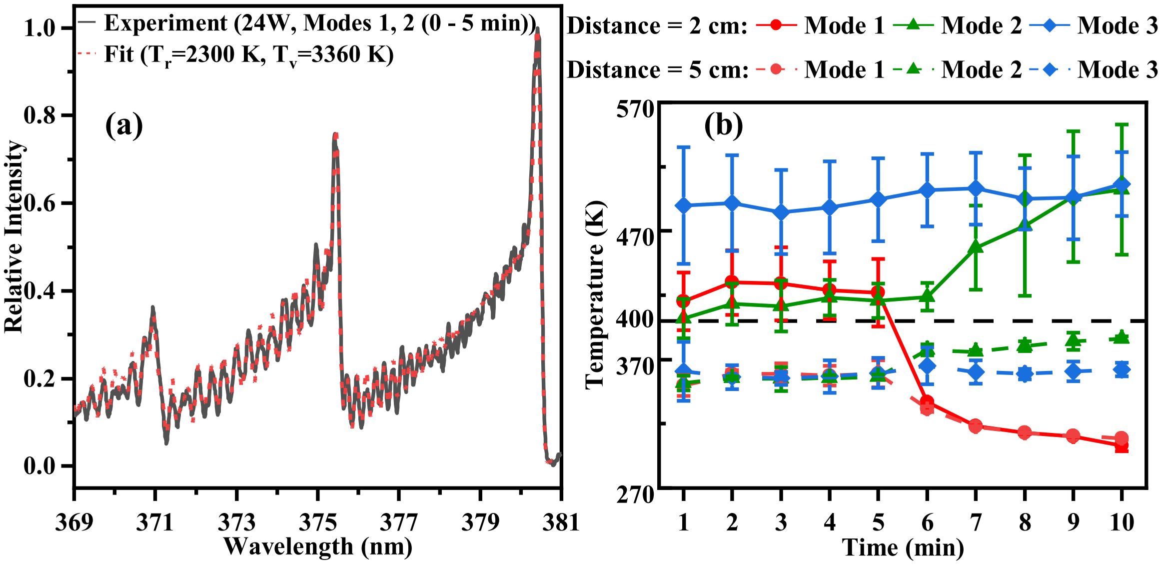

Fig. 5. Temperature change at 24 W. (a) is the gas temperature of Modes 1 and 2 (0–5 min) in plasma, and (b) is the temperature at different distances from the discharge region within the chamber.

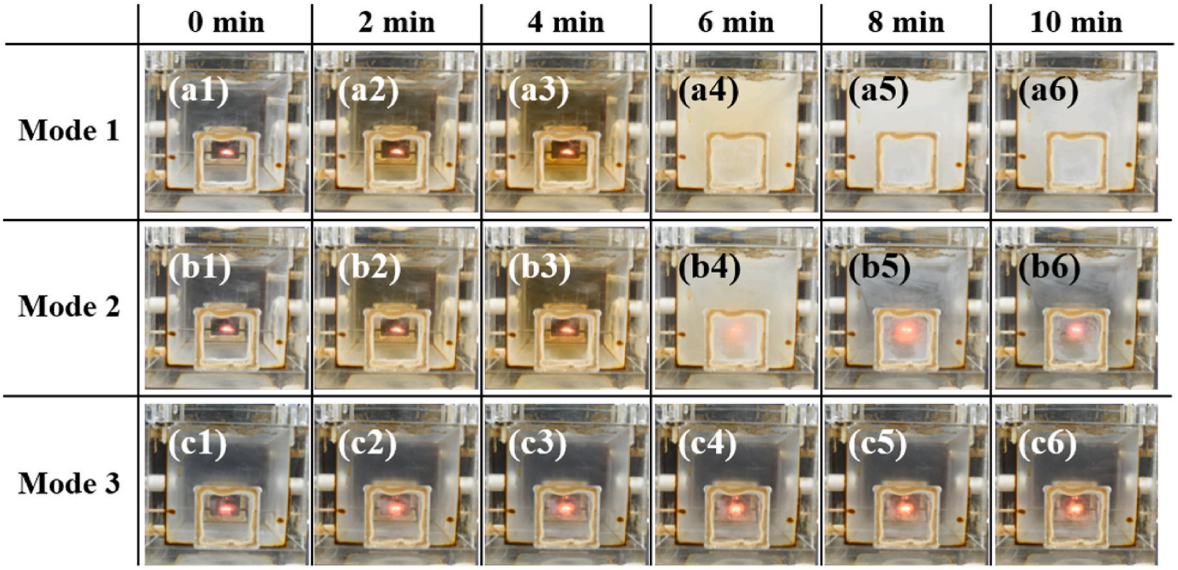

Fig. 6. The phenomena within the chamber with the discharge power of 24 W, working under (a) Mode 1, (b) Mode 2, and (c) Mode 3, respectively. (a1) ~ (a6), (b1) ~ (b6), and (c1) ~ (c6) represent the results obtained at 0 min, 2 min, 4 min, 6 min, 8 min, and 10 min of the process, respectively.

"white smoke" dominates the chamber. Under Mode 2, after 5 min, although "white smoke" appears, its production is significantly lower compared to Mode 1. Furthermore, no suspended particles are observed inside the chamber after 8 min, but some particles are observed on the chamber wall. In Mode 3 (as shown in Fig. 6 (c)), neither significant reddish-brown gas nor "white smoke" is observed throughout the entire process.

To validate the presence of the "white smoke" formed in the chamber, we conducted a series of analyses on the collected products. SEM images (shown in Fig. 7 (a)) reveal that particulate matter primarily exists as particles with dimensions ranging from 10 to 25 μm. The EDS mappings (Fig. 7 (b)) demonstrate that the solid products consist mainly of nitrogen (N) and oxygen (O), with an atomic ratio (At%) close to 2:3. This composition closely resembles that of NH_4NO_3, considering that

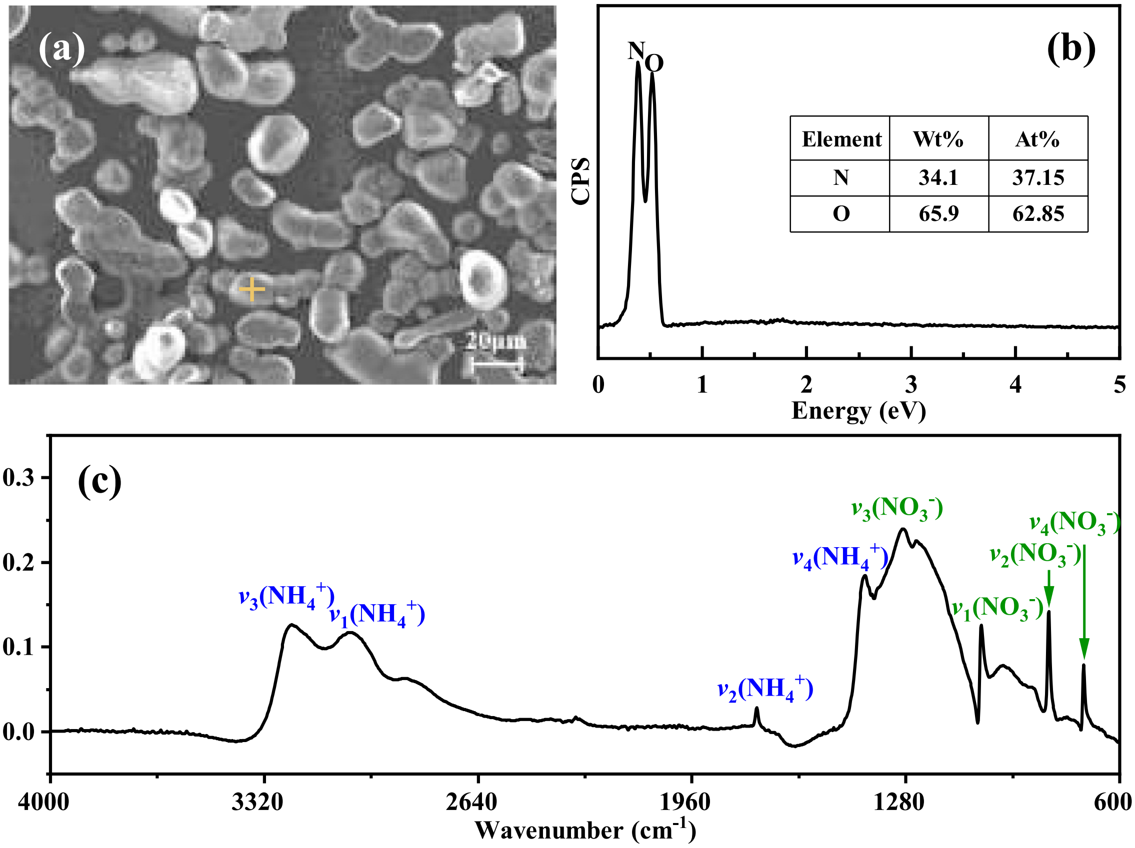

Element	Wt%	At%
N	34.1	37.15
O	65.9	62.85

Fig. 7. The detection results of the solid particles collected on the filter membrane. (a) SEM images, (b) EDS mappings (of which Wt% is the weight percentage and At% is the atom percentage), (c) ATR-FTIR spectra.

hydrogen (H) cannot be detected. ATR-FTIR spectra (Fig. 7 (c)) further confirm this finding, as the observed absorption bands are primarily attributed to the vibrational modes of NH_4^+ and NO_3^- in pure crystalline NH_4NO_3 (Schuttlefield et al., n.d.). In summary, through multiple validations, it is confirmed that NH_4NO_3 is the primary component of the “white smoke” generated during the experiment, which is further verified by the gas phase FTIR results in the following sections. From the results of the recorded images and the FTIR in all the reaction modes, it is found that the evolution of the white smoke inside the reaction chamber is in agreement with that of the new gas phase FTIR peak.

3.3. Revolution of gas-phase products

Fig. 8 illustrates the FTIR spectra and real-time concentrations of the gas-phase products in Mode 1. Within 0–5 min of both Mode 1 and Mode 2, the predominant gas-phase products are NO (at 1800–1950 cm^{-1}), NO_2 (at 1550–1675 cm^{-1}), (Liang et al., 2020) HNO_2 (at 1675–1750 cm^{-1}), and HNO_3 (at 1250–1475 cm^{-1}) (Goodman et al., 1999; Kirchner et al., 2000; Mochida and Finlayson-Pitts, 2000) (detailed FTIR spectra obtained during the first 5 min could be found in Appendix B). The concentrations of these species gradually increase with the duration of discharge. New FTIR peaks within the range of 1250–1500 cm^{-1} emerge under all discharge powers, which are identified as NH_4NO_3. The NO_x concentration exhibits an increase with the discharge power during 0–5 min. Following the shut-off of the discharge, the injection of NH_3 leads to a decrease in the NO_x concentration, indicating the occurrence of reactions between NO_x and NH_3. The concentration of NO_2 initially rises, followed by a subsequent decline. The initial rise is possibly due to the oxidation of NO into NO_2, while the decline is mainly due to the reaction with NH_3. The absorbance of the new peak NH_4NO_3 increases with both discharge power and reaction time, showing a slight decrease at 10 min.

It can be seen that in Mode 1, NH_4NO_3 can be produced and remains stable under various discharge powers. In this reaction mode, NH_3 does not directly interact with the plasma but is captured by gas-phase products after the air discharge is turned off. Initially, discharge occurs in an air environment consisting predominantly of N_2, O_2, and H_2O for the first 0–5 min, resulting in reactions (1)–(10) (Brisset and Pawlat, 2016; Hu et al., 2005; Trunec et al., 2022).

$$e + O_2 \rightarrow O + O + e \tag{1}$$

$$e + N_2 \rightarrow N + N + e \tag{2}$$

$$e + H_2O \rightarrow OH + H + e \tag{3}$$

$$N + O \rightarrow NO \tag{4}$$

$$N + O_2 \rightarrow NO + O \tag{5}$$

$$N_2 + O \rightarrow NO + N \tag{6}$$

$$NO + O \rightarrow NO_2 \tag{7}$$

$$NO + H_2O \rightarrow NO_2 + OH \tag{8}$$

$$NO + OH \rightarrow HNO_2 \tag{9}$$

$$NO_2 + OH \rightarrow HNO_3 \tag{10}$$

These reactions generate mainly NO, NO_2, HNO_2, and HNO_3 as after-plasma gas phase products. Following the injection of NH_3 at 5–10 min, the predominant formation reaction of NH_4NO_3 (and NH_4NO_2) occurs, as shown in equations (11)–(15) (Kim et al., 2001; Lin et al., 2006; Ono and Oda, 2008).

$$NH_3 + HNO_2 \rightarrow NH_4NO_2 \tag{11}$$

$$NH_3 + HNO_3 \rightarrow NH_4NO_3 \tag{12}$$

$$NH_3 + OH + NO \rightarrow NH_4NO_2 \tag{13}$$

$$NH_3 + OH + NO_2 \rightarrow NH_4NO_3 \tag{14}$$

$$2NH_3 + 2NO_2 + H_2O \rightarrow NH_4NO_3 + NH_4NO_2 \tag{15}$$

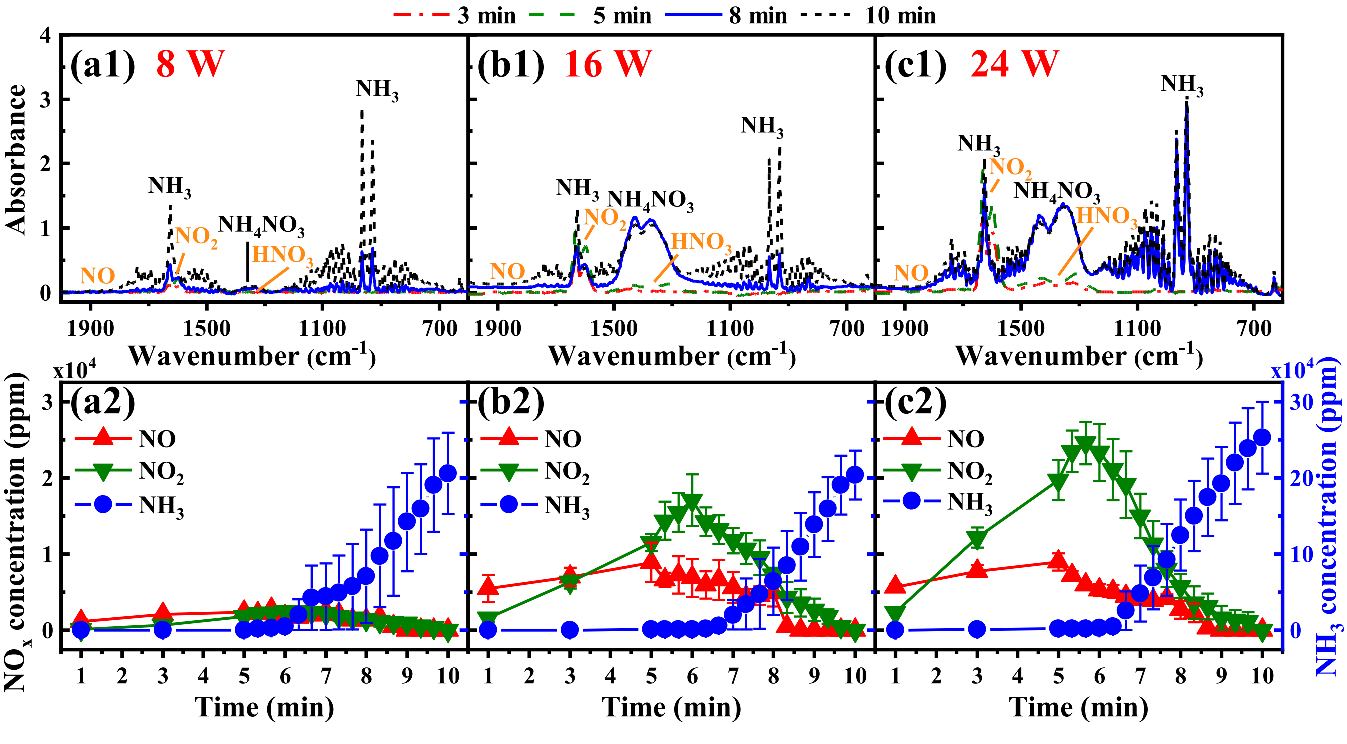

Fig. 8. FTIR spectra and real-time concentrations of gas-phase products under Mode 1. (a1) and (a2): 8 W; (b1) and (b2): 16 W; (c1) and (c2): 24 W.

NH_4NO_2 cannot remain stable at room temperature and decomposes through reaction (16).

$$NH_4NO_2 \rightarrow N_2 + H_2O \tag{16}$$

Since the temperature in the most space area of the chamber does not reach the thermal decomposition temperature (~400 K) (Babrauskas and Leggett, 2020) of NH_4NO_3 (as shown in Fig. 5 (b)), the decomposition reaction of NH_4NO_3 does not occur, ensuring the stable formation of NH_4NO_3.

Fig. 9 shows the FTIR spectra and real-time concentrations of the gas-phase products in Mode 2. The concentration of NO and NO_2 exhibits an initial increase until 6–8 min, followed by a subsequent decrease. The NO_x concentration does not immediately decrease with the injection of NH_3, but stabilizes for 1–3 min, possibly related to the continuous production of NO_x by the discharge. At the turning point, the concentration of NH_3 starts to significantly increase, suggesting a possible transition from air-dominated discharge to NH_3-dominated discharge. It is observed that NH_4NO_3 is generated under the discharge power of 16 W and 24 W, but different from Mode 1, all of the possible NH_4NO_3 peaks almost disappear at 10 min. The generation of NH_4NO_3 is not visibly observed and detected by FTIR at 8 W. Similar to Mode 1, it is found that higher discharge power results in increased production of both NO_x and NH_4NO_3 during the process.In Mode 2, NH_4NO_3 is initially produced and then rapidly decreased. The main reactions during the initial 0–5 min in Mode 2 are the same as those in Mode 1. After NH_3 is injected into the chamber, the reactions (1)–(10) continue, but the formation reactions (17)–(29) gradually become the predominant reaction (D'agostino et al., 1981; Nicholas et al., 1986).

$$e + NH_3 \rightarrow NH_2 + H + e \tag{17}$$

$$e + NH_3 \rightarrow NH + H_2 + e \tag{18}$$

$$e + NH_3 \rightarrow NH + H + H + e \tag{19}$$

$$NH_3 + H \rightarrow NH_2 + H_2 \tag{20}$$

$$NH_3 + OH \rightarrow NH_2 + H_2O \tag{21}$$

$$NH_2 + NH_2 \rightarrow NH + NH_3 \tag{22}$$

$$NH_2 + NH_2 \rightarrow NH + NH + H_2 \tag{23}$$

$$NH_2 + OH \rightarrow NH + H_2O \tag{24}$$

$$NH_2 + H \rightarrow NH + H_2 \tag{25}$$

$$NH_2 \rightarrow NH + H \tag{26}$$

$$NH + NH \rightarrow N_2 + H_2 \tag{27}$$

$$NH \rightarrow N + H \tag{28}$$

$$OH + H \rightarrow H_2O \tag{29}$$

The $\cdot NH_2$ and $\cdot NH$ groups generated from the aforementioned reactions can react with NO_x, as shown in equations (30)–(32) (Ju et al., 2023a; Nishida et al., 2001; Yukimura et al., 2007), thereby consuming NO_x and inhibiting NH_4NO_3 formation through reactions (11)–(15).

$$NH_2 + NO \rightarrow N_2 + H_2O \tag{30}$$

$$NH_2 + NO \rightarrow OH + N_2H \tag{31}$$

$$NH + NO \rightarrow N_2 + OH \tag{32}$$

Concurrently, the temperature near the discharge region gradually reaches the thermal decomposition temperature of NH_4NO_3 (as shown in Fig. 5 (b)) due to the continuous discharge. Consequently, thermal decomposition reactions with different reaction temperatures (33)–(35) also occur (Babrauskas and Leggett, 2020; Chaturvedi and Dave, 2013; Feick and Hainer, 1954), leading to the inability of NH_4NO_3 to remain stable and its rapid decrease.

$$NH_4NO_3 \rightarrow NH_3 + HNO_3 \tag{33}$$

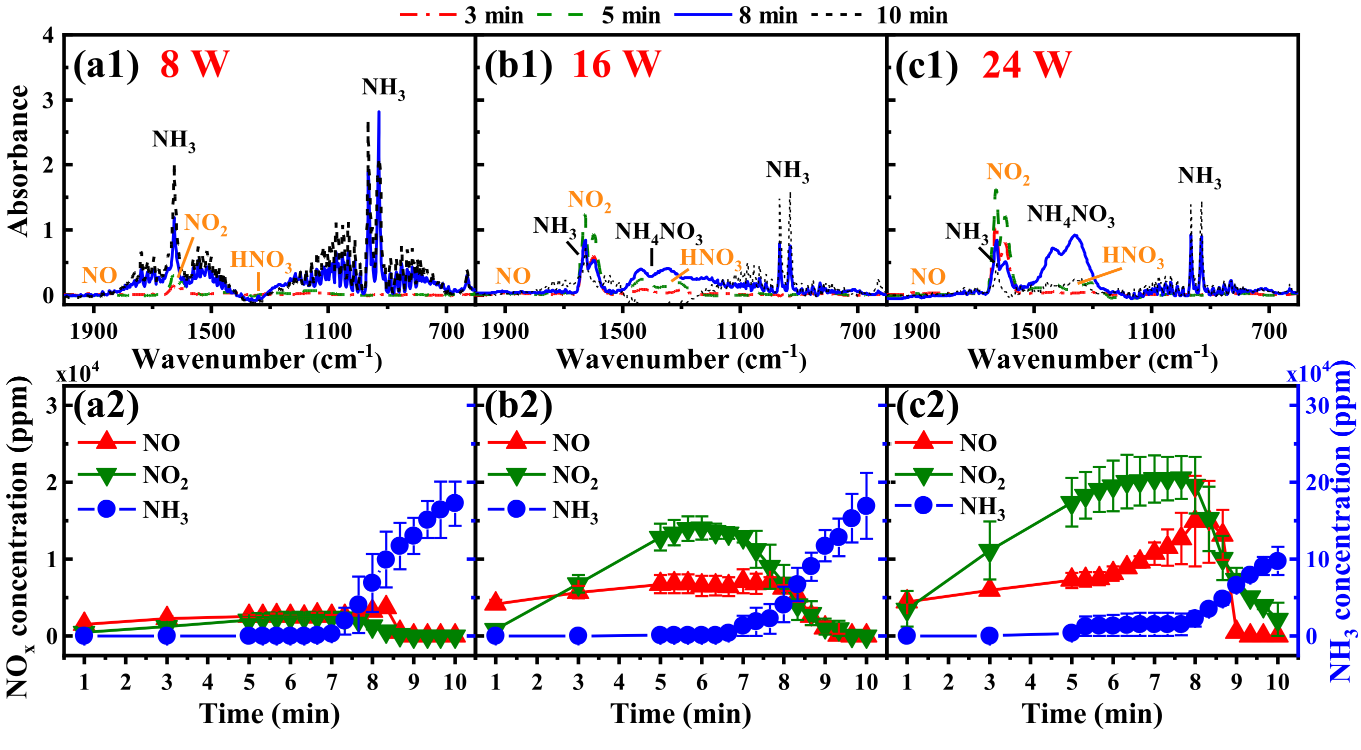

Fig. 9. FTIR spectra and real-time concentrations of major gases under Mode 2. (a1) and (a2): 8 W; (b1) and (b2): 16 W; (c1) and (c2): 24 W.

$$NH_4NO_3 \rightarrow N_2O + 2H_2O \tag{34}$$

$$2NH_4NO_3 \rightarrow 2N_2 + O_2 + 4H_2O \tag{35}$$

Fig. 10 shows the FTIR spectra and real-time concentrations of the gas-phase products in Mode 3. No other peaks, except for NH_3 (at 650–1250 and 1400–1850 cm^{-1}), are observed in Mode 3 under various power conditions. However, a slight distortion in the peak shape of NH_3 is observed, possibly attributed to the presence of small amounts of NO_x production. Due to the relatively low yield, these NO_x byproducts are overshadowed by the absorption peak of NH_3. The reason is that NH_3 is more easily decomposed by plasma compared to air. At the beginning of discharging, a significant decrease in the NH_3 concentration occurs at discharge powers of 16 W and 24 W, with a more pronounced decrease at 24W, while no significant change is observed at 8 W. As time progresses, the NH_3 concentration in the chamber gradually stabilizes.

In Mode 3, the air/NH_3 mixture is used with continuous discharge throughout the process, and no NH_4NO_3 formation is observed. The reactions are similar to those in Mode 2 but differ in the temporal sequence and the dominant reactions involved. Unlike Modes 1 and 2, no accumulation of NO_x occurs initially in Mode 3. NH_3 is decomposed by discharge, forming $\cdot NH_2$ or $\cdot NH$ groups. Reactions (1)–(10) and (17)–(29) occur simultaneously, with the latter being the predominant reactions. The production of NO_x is very low, and decomposition reactions (33)–(35) take place concurrently. Moreover, $\cdot NH_2$ and $\cdot NH$ will react with potential NO_x (Nishida et al., 2001; Yukimura et al., 2007) and suppress its accumulation (Ju et al., 2023b), further inhibiting NH_4NO_3 formation. Therefore, to efficiently produce NH_4NO_3 by capturing volatilized NH_3 using low-temperature plasma, it is crucial to prevent the decomposition of NH_3 by discharge and the thermal decomposition of NH_4NO_3.

3.4. Revolution of NH_4NO_3 yield in various conditions

Fig. 11 (a) and (b) illustrate the yield of NH_4NO_3 in Mode 1 and Mode 2. The production of NH_4NO_3 in Mode 1 is significantly higher compared to Mode 2. In Mode 1, the mass of NH_4NO_3 collected on the filter membrane increases sharply with the increase in discharge power, reaching its highest yield at 8 min, with a slight decrease at 10 min. This trend aligns with the findings from the FTIR analysis. Initially, the formation of NH_4NO_3 increases, while the NO_x concentration, temperature, and formation rate of NH_4NO_3 gradually decrease. One possible reason here is that the amount of NH_4NO_3 attached to the chamber wall exceeds the newly formed NH_4NO_3 after 8 min, resulting in a reduction in the collected mass. The yield of particles attached to the chamber walls increases with time and is relatively small compared to the total yield. Taking the example of a discharge power of 24 W, even at 10 min, the yield on the chamber walls only accounts for 5%–9% of the final yield, indicating a minor impact. If adding the mass attached on the chamber walls to the mass collected on the filter membrane, the total yields of NH_4NO_3 at 10 min and 8 min are very close. In Mode 2, NH_4NO_3 could also be collected under the three discharge powers; however, the collected NH_4NO_3 gradually decreases with the increase of discharge time. There are nearly no particles collected from the chamber wall in Mode 2. Although the mass of NH_4NO_3 increases at 6 min with the discharge power, the high temperature during discharge leads to the thermal decomposition of NH_4NO_3, resulting in a relatively lower yield compared to Mode 1. The maximum mass of collected NH_4NO_3 in Mode 2 is approximately 5 times lower than that in Mode 1.

To further explore the effect of NH_3 flow rate (NH_3 concentration) on the final NH_4NO_3 yield, we conducted additional experiments by changing the NH_3 flow rate under the optimal conditions of Mode 1 and 24W discharge power, as shown in Fig. 11(c), where NH_4NO_3 was collected at the time point of 10 min. It can be seen that as the NH_3 flow rate gradually increases from 1 sccm to 80 sccm, the NH_4NO_3 mass first increases and then decreases, reaching a maximum value at 20 sccm. The reason for the high NH_4NO_3 yield at 20sccm NH_3 flow rate may be that the relatively slow flow rate results in a longer residence time for the reactants inside the chamber, leading to more adequate reactions and higher NH_4NO_3 yield (Chang et al., 2021; Zhu et al., 2016). The

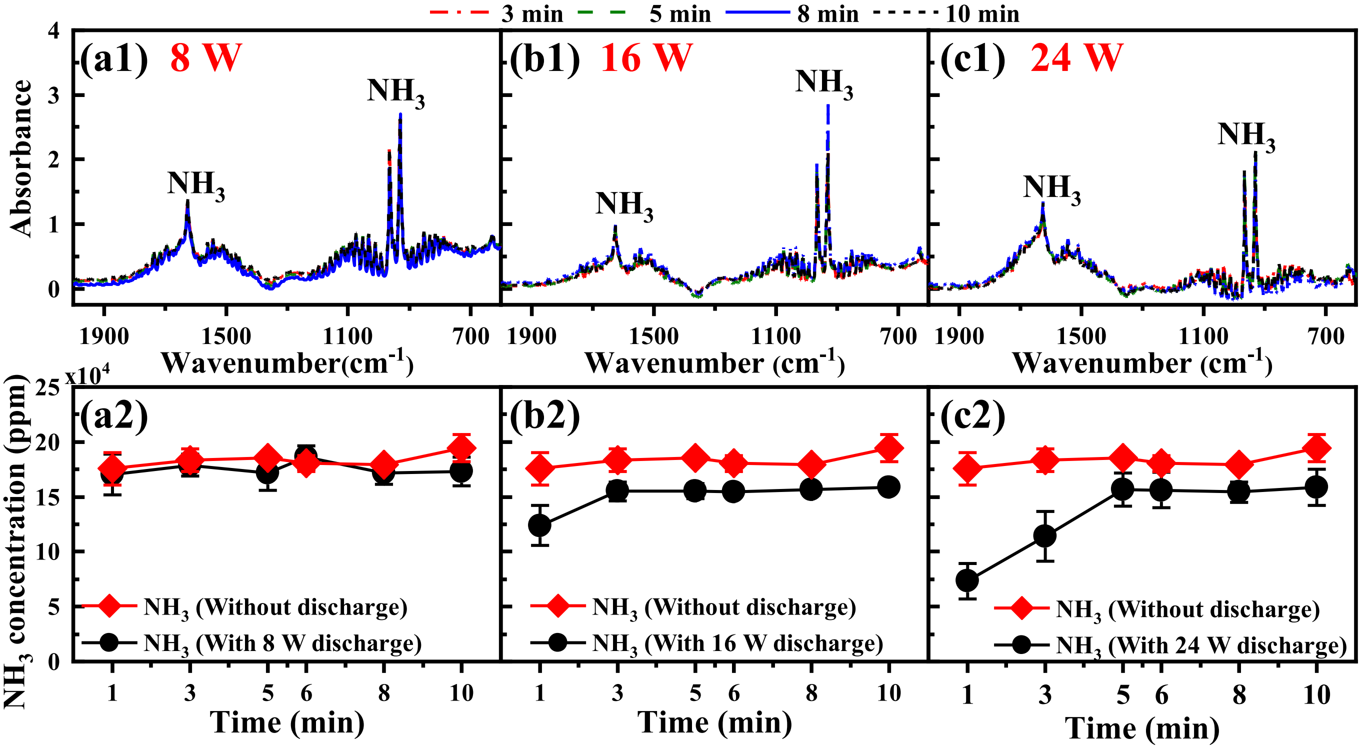

Fig. 10. FTIR spectra and real-time concentrations of NH_3 under Mode 2 (a1) and (a2): 8 W; (b1) and (b2): 16 W; (c1) and (c2): 24 W.

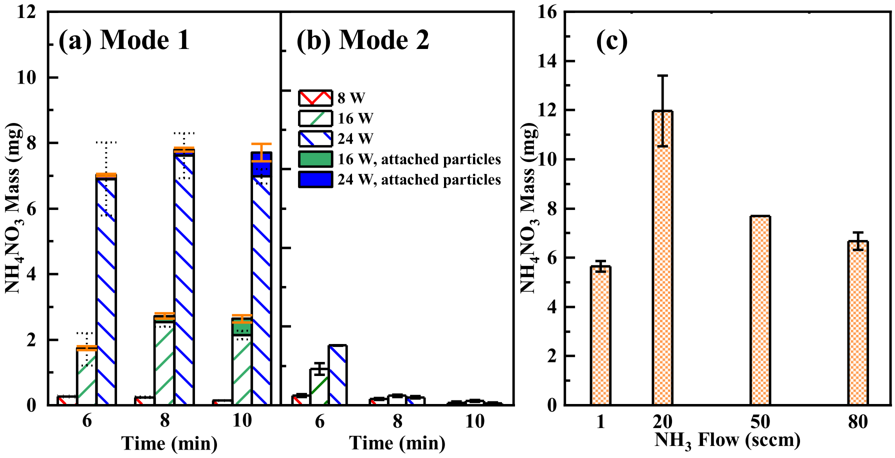

Fig. 11. The mass evolution of NH_4NO_3. (a) Mode 1 and (b) Mode 2 are of the same NH_3 flow of 80 sccm under different discharge power and experiment time. (c) The collected mass under different NH_3 flow rates in Mode 1 with the discharge power of 24 W at the time point of 10min.

subsequent decrease in yield at a higher flow rate is mainly due to the reduced residence time. At 1 sccm flow rate after 5 min of NH_3 flow, the NH_3 was completely captured, however, due to the insufficient NH_3 content in the reaction chamber to react with NO_x, the NO_x was not fully reacted and caused the reduced NH_4NO_3 yield at the time point of 10 min.

Our proposed method utilizes air plasma for the capture of wasted NH_3, combining NH_3 pollution treatment and plasma nitrogen fixation. This approach not only effectively treats NH_3 pollution but also reduces the limitations of plasma nitrogen fixation, resulting in the efficient production of NH_4NO_3 for secondary use. The results demonstrate that NH_4NO_3 yield is highly dependent on NO_x concentration, reaction mode, plasma temperature, gas flow rate, and temperature distribution within the reaction chamber. Working in Mode 1 under suitable discharge power and NH_3 flow rate, effective capture of wasted NH_3 can be achieved, and these data could be used as a reference in practice, for example, when utilizing the proposed method in animal houses and manure storage areas. Given that the application scenario of this technology mainly targets livestock, which is typically located in open areas with sufficient solar or wind energy resources, combining with photovoltaic or wind power devices can further reduce energy consumption, achieve green and clean ammonia recovery as well as reduce ammonia emissions at relatively low costs.

4. Conclusion

N loss in the form of NH_3 from agriculture and livestock is the dominant way of N loss in the nitrogen cycle and results in significant resource waste and environmental pollution. In this study, we proposed and explored the way of using air plasma to capture wasted ammonia to form NH_4NO_3 for N recycling. Comprehensive investigations on the impact of reaction modes, discharge power as well as gas flow rate on the capture efficiency were conducted. The possible underlying mechanism involved in each reaction mode was also discussed. The efficiency of NH_4NO_3 generation was found to be significantly influenced by the interaction mode between plasma and NH_3, discharge power, the NH_3 flow rate, and the temperature inside the reaction chamber. Our findings revealed that the most effective approach for capturing NH_3 and generating NH_4NO_3 was the indirect reaction between post-plasma products and NH_3, without the presence of discharge. Under this mode, NH_4NO_3 yield increases with the discharge power and first increases and then decreases with the NH_3 flow rate, reaching a maximum NH_4NO_3 yield of ~12 mg at 24W and 20 sccm NH_3 flow rate in this study. Direct discharge in an air-NH_3 mixture was found to hinder and decompose the formation of NH_4NO_3. The discharge power will also affect the temperature distribution inside the reaction chamber, and it is crucial to control the temperature rise below the critical temperature of ~400 K (the threshold for thermal decomposition of NH_4NO_3), to achieve efficient generation and stable existence of NH_4NO_3. In our future research, we plan to further improve the NH_4NO_3 generation efficiency by considering additional factors such as air humidity, the ratio of air to NH_3, using catalyst, etc.

CRediT authorship contribution statement

Mengqi Li: Investigation, Methodology, Data curation, Writing – original draft. **Zhenguo Hou:** Investigation, Data curation. **Yi Dai:** Investigation. **Zhuocheng Song:** Investigation. **Zilan Xiong:** Conceptualization, Methodology, Resources, Supervision, Writing – review & editing.

Declaration of competing interest

The authors declare that they have no known competing financial interests or personal relationships that could have appeared to influence the work reported in this paper.

Data availability

Data will be made available on request.

Acknowledgement

The authors are grateful for financial support from the National Natural Science Foundation of China (No. 52177145).

Appendix A

Table. A.1
The gas temperature in plasma obtained by spectra fitting

Discharge Power	Modes 1, 2 (0–5 min)	Mode 2 (5–10 min)	Mode 3
8W	$T_r = 2170$ K, $T_v = 3532$ K	$T_r = 2300$ K, $T_v = 3522$ K	$T_r = 2258$ K, $T_v = 3343$ K
16W	$T_r = 2200$ K, $T_v = 3512$ K	$T_r = 2359$ K, $T_v = 3671$ K	$T_r = 2275$ K, $T_v = 3445$ K
24W	$T_r = 2300$ K, $T_v = 3360$ K	$T_r = 2500$ K, $T_v = 3874$ K	$T_r = 2439$ K, $T_v = 3631$ K

Here, T_r is the rotational temperature, and T_v is the vibrational temperature.

Appendix B

Figure B.1 shows the FTIR spectra obtained during the initial 5 min. Fig. B.1 (a) reveals that within 0–5 min of both Mode 1 and Mode 2, the predominant gas-phase products are NO (at 1800–1950 cm^{-1}), NO_2 (at 1550–1675 cm^{-1}), HNO_2 (at 1675–1750 cm^{-1}) and HNO_3 (at 1250–1475 cm^{-1}). The concentrations of these species gradually increase with the duration of discharge. Due to its high absorptivity, HNO_3 forms aerosol particles suspended within the chamber in the presence of water molecules, resulting in a slightly different absorption peak position compared to gaseous HNO_3. Fig. B.1 (b) indicates that the predominant gas-phase product in Mode 3 is NH_3 (at 650–1250 and 1400–1850 cm^{-1}).

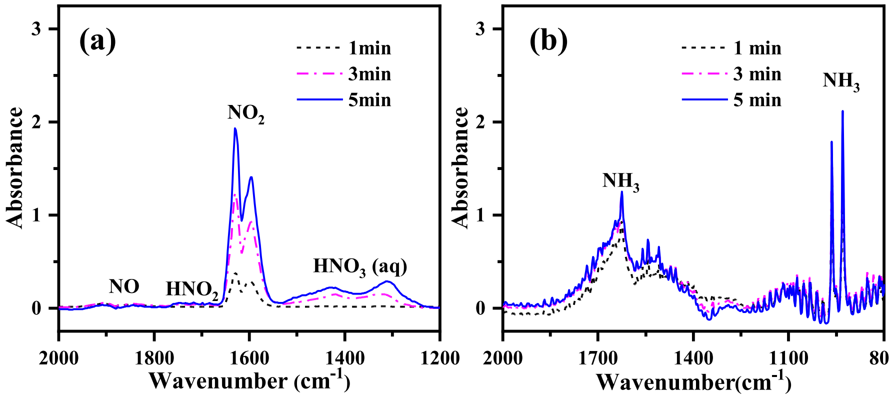

Fig. B.1. FTIR spectra obtained during the first 5 min of (a) Mode 1, 2, and (b) Mode 3. The notation HNO3 (aq) represents aqueous HNO_3.

References

Akay, G., 2017. Sustainable ammonia and advanced symbiotic fertilizer production using catalytic multi-reaction-zone reactors with nonthermal plasma and simultaneous reactive separation. ACS Sustain. Chem. Eng. 5 https://doi.org/10.1021/acssuschemeng.7b02962.

Anderson, N., Strader, R., Davidson, C., 2003. Airborne reduced nitrogen: ammonia emissions from agriculture and other sources. Environ. Int. https://doi.org/10.1016/S0160-4120(02)00186-1.

Babrauskas, V., Leggett, D., 2020. Thermal decomposition of ammonium nitrate. Fire Mater. 44, 250–268. https://doi.org/10.1002/fam.2797.

Back, S., Saito, N., Lee, S., 2023. A facile and efficient approach for the removal of high concentrations of ammonia nitrogen in wastewater: liquid-phase plasma treatment. J. Environ. Chem. Eng. 11 https://doi.org/10.1016/j.jece.2022.109075.

Bouwman, A.F., Beusen, A.H.W., Griffioen, J., Van Groenigen, J.W., Hefting, M.M., Oenema, O., Van Puijenbroek, P.J.T.M., Seitzinger, S., Slomp, C.P., Stehfest, E., 2013. Global trends and uncertainties in terrestrial denitrification and N2O emissions. Phil Trans. Roy. Soc. B: Biol. Sci. 368 https://doi.org/10.1098/rstb.2013.0112.

Brisset, J.L., Pawlat, J., 2016. Chemical effects of air plasma species on aqueous solutes in direct and delayed exposure modes: discharge, post-discharge and plasma activated water. Plasma Chem. Plasma Process. https://doi.org/10.1007/s11090-015-9653-6.

Bruggeman, P., Cunge, G., Sadeghi, N., 2012. Absolute OH density measurements by broadband UV absorption in diffuse atmospheric-pressure HeH 2O RF glow discharges. Plasma Sources Sci. Technol. 21 https://doi.org/10.1088/0963-0252/21/3/035019.

Chang, T., Chen, Q., Fan, H., Shen, Z., Zhang, B., Huang, Y., Veerapandian, S.K.P., De Geyter, N., Morent, R., 2021. Removal mechanism and quantitative control of trichloroethylene in a post-plasma-catalytic system over Mn–Ce/HZSM-5 catalysts. Catal. Sci. Technol. 11, 3746–3761. https://doi.org/10.1039/D1CY00141H.

Chaturvedi, S., Dave, P.N., 2013. Review on thermal decomposition of ammonium nitrate. J. Energetic Mater. 31, 1–26. https://doi.org/10.1080/07370652.2011.573523.

Chen, C.-J., Li, S.-Z., 2017. Investigation of a nitrogen post-discharge of an atmospheric-pressure microwave plasma torch by optical emission spectroscopy. Phys. Plasmas 24, 033512. https://doi.org/10.1063/1.4978948.

Chen, H., Yuan, D., Wu, A., Lin, X., Li, X., 2021. Review of low-temperature plasma nitrogen fixation technology. Waste Dispos. Sustain. Energy. https://doi.org/10.1007/s42768-021-00074-z.

Chojnacka, K., Mikula, K., Izydorczyk, G., Skrzypczak, D., Witek-Krowiak, A., Gersz, A., Moustakas, K., Iwaniuk, J., Grzędzicki, M., Korczyński, M., 2021. Innovative high digestibility protein feed materials reducing environmental impact through improved nitrogen-use efficiency in sustainable agriculture. J. Environ. Manag. https://doi.org/10.1016/j.jenvman.2021.112693.

Chung, K.H., Park, Y.K., Jung, S.C., 2022. Hydrogen production by cracking of ammonium hydroxide using liquid-phase plasma on the modified TiO2 photocatalysts. Int. J. Hydrogen Energy 47. https://doi.org/10.1016/j.ijhydene.2022.06.032.

Cicala, G., De Tommaso, E., Rainò, A.C., Lebedev, Y.A., Shakhatov, V.A., 2009. Study of positive column of glow discharge in nitrogen by optical emission spectroscopy and numerical simulation. Plasma Sources Sci. Technol. 18 https://doi.org/10.1088/0963-0252/18/2/025032.

Clay, K.J., Speakman, S.P., Amaratunga, G.A.J., Silva, S.R.P., 1996. Characterization of a-C:H:N deposition from CH4/N2 rf plasmas using optical emission spectroscopy. J. Appl. Phys. 79, 7227–7233. https://doi.org/10.1063/1.361439.

Congreves, K.A., Otchere, O., Ferland, D., Farzadfar, S., Williams, S., Arcand, M.M., 2021. Nitrogen use efficiency definitions of today and tomorrow. Front. Plant Sci. 12 https://doi.org/10.3389/fpls.2021.637108.

D'agostino, R., Cramarossa, F., De Benedictis, S., Ferraro, G., 1981. Kinetic and spectroscopic analysis of NH3 decomposition under R.F. Plasma at moderate pressures. Plasma Chem. Plasma Process. https://doi.org/10.1007/BF00566373.

Engeln, R., Klarenaar, B., Guaitella, O., 2020. Foundations of optical diagnostics in low-temperature plasmas. Plasma Sources Sci. Technol. 29, 063001 https://doi.org/10.1088/1361-6595/ab6880.

Es-Sebbar, E., Benilan, Y., Jolly, A., Gazeau, M.C., 2009. Characterization of an N2 flowing microwave post-discharge by OES spectroscopy and determination of absolute ground-state nitrogen atom densities by TALIF. J. Phys. D Appl. Phys. 42 https://doi.org/10.1088/0022-3727/42/13/135206.

Fan, J., Wu, H., Liu, R., Meng, L., Fang, Z., Liu, F., Xu, Y., 2021. Non-thermal plasma combined with zeolites to remove ammonia nitrogen from wastewater. J. Hazard Mater. 401, 123627 https://doi.org/10.1016/j.jhazmat.2020.123627.

Feick, G., Hainer, R.M., 1954. On the thermal decomposition of ammonium nitrate. Steady-State reaction temperatures and reaction rate. J. Am. Chem. Soc. 76 https://doi.org/10.1021/ja01651a096.

Fowler, D., Coyle, M., Skiba, U., Sutton, M.A., Cape, J.N., Reis, S., Sheppard, L.J., Jenkins, A., Grizzetti, B., Galloway, J.N., Vitousek, P., Leach, A., Bouwman, A.F., Butterbach-Bahl, K., Dentener, F., Stevenson, D., Amann, M., Voss, M., 2013. The global nitrogen cycle in the Twenty-first century. Phil Trans. Roy. Soc. B: Biol. Sci. 368 https://doi.org/10.1098/rstb.2013.0164.

Fowler, D., Steadman, C.E., Stevenson, D., Coyle, M., Rees, R.M., Skiba, U.M., Sutton, M.A., Cape, J.N., Dore, A.J., Vieno, M., Simpson, D., Zaehle, S., Stocker, B.D., Rinaldi, M., Facchini, M.C., Flechard, C.R., Nemitz, E., Twigg, M., Erisman, J.W., Butterbach-Bahl, K., Galloway, J.N., 2015. Effects of global change during the 21st century on the nitrogen cycle. Atmos. Chem. Phys. https://doi.org/10.5194/acp-15-13849-2015.

Galloway, J.N., Dentener, F.J., Capone, D.G., Boyer, E.W., Howarth, R.W., Seitzinger, S.P., Asner, G.P., Cleveland, C.C., Green, P.A., Holland, E.A., Karl, D.M., Michaels, A.F., Porter, J.H., Townsend, A.R., Vörösmarty, C.J., 2004. Nitrogen cycles: past, present, and future. Biogeochemistry 70. https://doi.org/10.1007/s10533-004-0370-0.

Goodman, A.L., Underwood, G.M., Grassian, V.H., 1999. Heterogeneous reaction of NC2: characterization of gas-phase and adsorbed products from the reaction, 2NO2(g) + H2O(a) → HONO(g) + HNO3(a) on hydrated silica particles. J. Phys. Chem. A 103, 7217–7223. https://doi.org/10.1021/jp9910688.

Hong, J., Prawer, S., Murphy, A.B., 2018. Plasma catalysis as an alternative route for ammonia production: status, mechanisms, and prospects for progress. ACS Sustain. Chem. Eng. https://doi.org/10.1021/acssuschemeng.7b02381.

Hu, X., Zhao, G.-B., Legowski, S.F., Radosz, M., 2005. Moisture effect on NOx conversion in a nonthermal plasma reactor. Environ. Eng. Sci. https://doi.org/10.1089/ees.2005.22.854.

Humphreys, J., Lan, R., Tao, S., 2021. Development and recent progress on ammonia synthesis catalysts for Haber–Bosch process. Adv. Energy Sustain. Res. 2 https://doi.org/10.1002/aesr.202000043.

Ju, R., Wang, J., Zhang, M., Mu, H., Wu, Y., Zhang, G., Huang, Z., 2023a. Experimental study on burning velocity, structure, and NOx emission of premixed laminar and swirl NH3/H2/air flames assisted by non-thermal plasma. Appl. Energy Combust. Sci. 14, 100149 https://doi.org/10.1016/j.jaecs.2023.100149.

Ju, R., Wang, J., Zhang, M., Mu, H., Zhang, G., Yu, J., Huang, Z., 2023b. Stability and emission characteristics of ammonia/air premixed swirling flames with rotating gliding arc discharge plasma. Energy 277, 127649. https://doi.org/10.1016/j.energy.2023.127649.

Kim, H.H., Takashima, K., Katsura, S., Mizuno, A., 2001. Low-temperature NOx reduction processes using combined systems of pulsed corona discharge and catalysts. J. Phys. D Appl. Phys. 34 https://doi.org/10.1088/0022-3727/34/4/322.

Kirchner, U., Scheer, V., Vogt, R., 2000. FTIR spectroscopic investigation of the mechanism and kinetics of the heterogeneous reactions of NO2 and HNO3 with soot. J. Phys. Chem. A 104, 8908–8915. https://doi.org/10.1021/jp0005322.

Liang, J.P., Zhao, Z.L., Zhou, X.F., Yang, D.Z., Yuan, H., Wang, W.C., Qiao, J.J., 2020. Comparison of gas phase discharge and gas-liquid discharge for water activation and methylene blue degradation. Vacuum 181. https://doi.org/10.1016/j.vacuum.2020.109644.

Lin, Y.C., Cheng, M.T., Ting, W.Y., Yeh, C.R., 2006. Characteristics of gaseous HNO2, HNO3, NH3 and particulate ammonium nitrate in an urban city of Central Taiwan. Atmos. Environ. 40 https://doi.org/10.1016/j.atmosenv.2006.04.037.

Lofthus, A., Krupenie, P.H., 1977. The spectrum of molecular nitrogen. J. Phys. Chem. Ref. Data 6, 113–307. https://doi.org/10.1063/1.555546.

Machala, Z., Janda, M., Hensel, K., Jedlovský, I., Leštinská, L., Foltin, V., Martišovitš, V., Morvová, M., 2007. Emission spectroscopy of atmospheric pressure plasmas for bio-medical and environmental applications. J. Mol. Spectrosc. 243, 194–201. https://doi.org/10.1016/j.jms.2007.03.001.

Mayerhöfer, T.G., Pahlow, S., Popp, J., 2020. The Bouguer-Beer-Lambert law: shining light on the obscure. ChemPhysChem. https://doi.org/10.1002/cphc.202000464.

Mei, D., Tu, X., 2017. Conversion of CO2 in a cylindrical dielectric barrier discharge reactor: effects of plasma processing parameters and reactor design. J. CO2 Util. 19 https://doi.org/10.1016/j.jcou.2017.02.015.

Mochida, M., Finlayson-Pitts, B.J., 2000. FTIR studies of the reaction of gaseous NO with HNO3 on porous glass: implications for conversion of HNO3 to photochemically active NOx in the atmosphere. J. Phys. Chem. A 104, 9705–9711. https://doi.org/10.1021/jp001471a.

Nicholas, J.E., Spiers, A.I., Martin, N.A., 1986. Kinetics and mechanism in the decomposition of NH3 in a radio-frequency pulse discharge. Plasma Chem. Plasma Process. https://doi.org/10.1007/BF00573820.

Nishida, M., Yukimura, K., Kambara, S., Maruyama, T., 2001. NO x removal using ammonia radicals prepared by intermittent dielectric barrier discharge at atmospheric pressure. Jpn. J. Appl. Phys. https://doi.org/10.1143/jjap.40.1114.

Nishio, M., Akita, S., Nakayama, Y., 2004. Cooling effect on the growth of carbon nanotubes and optical emission spectroscopy in short-period arc-discharge. Thin Solid Films 464–465. https://doi.org/10.1016/j.tsf.2004.06.068.

Ono, R., Oda, T., 2008. Measurement of gas temperature and OH density in the afterglow of pulsed positive corona discharge. J. Phys. D Appl. Phys. 41 https://doi.org/10.1088/0022-3727/41/3/035204.

Panetta, D.M., Powers, W.J., Lorimor, J.C., 2005. Management strategy impacts on ammonia volatilization from swine manure. J. Environ. Qual. 34 https://doi.org/10.2134/jeq2004.0313.

Park, J., Kim, E., Oh, S., Kim, H., Kim, S., Kim, Y.P., Song, M., 2021. Contributions of ammonia to high concentrations of pm2.5 in an urban area. Atmosphere (Basel) 12. https://doi.org/10.3390/atmos12121676.

Patil, B.S., Wang, Q., Hessel, V., Lang, J., 2015. Plasma N2-fixation: 1900–2014. Catal. Today 256. https://doi.org/10.1016/j.cattod.2015.05.005.

Pei, X., Gidon, D., Yang, Y.J., Xiong, Z., Graves, D.B., 2019. Reducing energy cost of NOx production in air plasmas. Chem. Eng. J. 362, 217–228. https://doi.org/10.1016/j.cej.2019.01.011.

Peng, P., Chen, P., Schiappacasse, C., Zhou, N., Anderson, E., Chen, D., Liu, J., Cheng, Y., Hatzenbeller, R., Addy, M., Zhang, Y., Liu, Y., Ruan, R., 2018. A review on the non-thermal plasma-assisted ammonia synthesis technologies. J. Clean. Prod. https://doi.org/10.1016/j.jclepro.2017.12.229.

Schuttlefield, J., Al-Hosney, H., Zachariah, A., Grassian, V.H.. n.d. Attenuated Total Reflection Fourier Transform Infrared Spectroscopy to Investigate Water Uptake and Phase Transitions in Atmospherically Relevant Particles. https://doi.org/10.1366/000370207780220868..

Suraj, K.S., Bharathi, P., Prahlad, V., Mukherjee, S., 2007. Near cathode optical emission spectroscopy in N2-H2 glow discharge plasma. Surf. Coat. Technol. 202, 301–309. https://doi.org/10.1016/j.surfcoat.2007.05.063.

Tanthapanichakoon, W., Charinpanitkul, T., Chaiyo, S., Dhattavorn, N., Chaichanawong, J., Sano, N., Tamon, H., 2004. Effect of oxygen and water vapor on the removal of styrene and ammonia from nitrogen by non-pulse corona-discharge at elevated temperatures. Chem. Eng. J. 97, 213–223. https://doi.org/10.1016/S1385-8947(03)00212-2.

Trunec, D., Navrátil, Z., Tomeková, J., Mazánková, V., Ďurčányová, S., Zahoranová, A., 2022. Chemical composition of gaseous products generated by coplanar barrier discharge in air and N2/O2 mixtures. Plasma Sources Sci. Technol. 31 https://doi.org/10.1088/1361-6595/ac9c8f.

Vervloessem, E., Gromov, M., De Geyter, N., Bogaerts, A., Gorbanev, Y., Nikiforov, A., 2023. NH3 and HNOx formation and loss in nitrogen fixation from air with water vapor by nonequilibrium plasma. ACS Sustain. Chem. Eng. 11 https://doi.org/10.1021/acssuschemeng.3c00208.

Wang, L., Yi, Y., Zhao, Y., Zhang, R., Zhang, J., Guo, H., 2015. NH3 decomposition for H2 generation: effects of cheap metals and supports on plasma-catalyst synergy. ACS Catal. 5 https://doi.org/10.1021/acscatal.5b00728.

Wu, H., Fan, J., Sun, Y., Liu, R., Jin, J., Li, P., 2021. Removal of ammonia nitrogen and phenol by pulsed discharge plasma combined with modified zeolite catalyst. J. Environ. Manag. 299 https://doi.org/10.1016/j.jenvman.2021.113590.

Xia, L., Huang, L., Shu, X., Zhang, R., Dong, W., Hou, H., 2008. Removal of ammonia from gas streams with dielectric barrier discharge plasmas. J. Hazard Mater. 152 https://doi.org/10.1016/j.jhazmat.2007.06.070.

Xie, Q., Zhuge, S., Song, X., Lu, M., Yu, F., Ruan, R., Nie, Y., 2020. Non-thermal atmospheric plasma synthesis of ammonia in a DBD reactor packed with various catalysts. J. Phys. D Appl. Phys. 53 https://doi.org/10.1088/1361-6463/ab57e5.

Yi, Y., Zhang, R., Wang, L., Yan, J., Zhang, J., Guo, H., 2017. Plasma-triggered CH4/NH3 coupling reaction for direct synthesis of liquid nitrogen-containing organic chemicals. ACS Omega 2, 9199–9210. https://doi.org/10.1021/acsomega.7b01060.

Yukimura, K., Kawamura, K., Hiramatsu, T., Murakami, H., Kambara, S., Moritomi, H., Yamashita, T., 2007. Efficient decomposition of NO by ammonia radical-injection method using an intermittent dielectric barrier discharge. Thin Solid Films 515, 4278–4282. https://doi.org/10.1016/j.tsf.2006.02.069.

Zhang, J., Wang, Q., 2016. Sustainable mechanisms of biochar derived from brewers' spent grain and sewage sludge for ammonia-nitrogen capture. J. Clean. Prod. 112 https://doi.org/10.1016/j.jclepro.2015.07.096.

Zhou, D., Zhou, Renwu, Zhou, Rusen, Liu, B., Zhang, T., Xian, Y., Cullen, P.J., Lu, X., Ostrikov, K. (Ken), 2021. Sustainable ammonia production by non-thermal plasmas: status, mechanisms, and opportunities. Chem. Eng. J. https://doi.org/10.1016/j.cej.2021.129544.

Zhu, X., Liu, S., Cai, Y., Gao, X., Zhou, J., Zheng, C., Tu, X., 2016. Post-plasma catalytic removal of methanol over Mn–Ce catalysts in an atmospheric dielectric barrier discharge. Appl. Catal., B 183, 124–132. https://doi.org/10.1016/j.apcatb.2015.10.013.